Laser path engineering of microstructure and multi-properties in additively manufactured high-silicon steel

Downloaded from: https://research.chalmers.se, 2026-11-10 09:33 UTC

Citation for the original published paper (version of record):
Murali, M., Hryha, E., Klement, U. et al (2026). Laser path engineering of microstructure and multi-properties in additively manufactured
high-silicon steel. MRS Bulletin, 51(9): 1133-1144. http://dx.doi.org/10.1557/s43577-026-01142-7

N.B. When citing this work, cite the original published paper.

research.chalmers.se offers the possibility of retrieving research publications produced at Chalmers University of Technology. It covers all kind of research output: articles, dissertations, conference papers, reports etc. since 2004. research.chalmers.se is administrated and maintained by Chalmers Library

(article starts on next page)

Laser path engineering of microstructure and multi-properties in additively manufactured high-silicon steel

Mukesh Murali, Eduard Hryha, Uta Klement, and Varun Chaudhary*

Received: 26 March 2026 / Revised: 22 May 2026 / Accepted: 4 June 2026 /
Published online: 6 July 2026

The influence of laser path rotation on the microstructure and multifunctional properties of high-silicon steel fabricated by powder bed fusion-laser beam was investigated using a high-throughput approach. Four laser path rotation angles were incorporated within a single build to directly correlate processing, structure, and coupled properties. Grain morphology and crystallographic texture were strongly governed by the laser path. A 90° rotation promoted elongated columnar grains with a pronounced ⟨001⟩ fiber texture along the build direction, whereas the 0° condition produced narrower columnar grains with largely random orientation. These variations resulted in distinct functional responses: the as-printed 90° condition exhibited the lowest coercivity of 81 A/m, while the 0° condition showed the highest electrical resistivity of 228 μΩ·cm and hardness of 416 HV. Annealing at 1150°C reduced coercivity to ~35 A/m while retaining high magnetization and elevated resistivity. These findings demonstrate that laser path engineering enables tunable magnetic, electrical, and mechanical performance in high-silicon steel.

Impact statement

Additive manufacturing is often associated with geometric freedom, but its deeper potential lies in controlling how materials solidify and evolve. This work shows that laser path design can be used to program microstructure within a single material, without altering composition. By isolating laser path rotation within a single build, a clear link is established between scan strategy, crystallographic texture, grain morphology, and functional response. The results highlight how texture alignment and grain-boundary density govern domain wall motion and electrical transport in Fe–6.5 wt% Si.

This shifts process-path design from a secondary parameter to a primary tool for materials engineering, comparable to composition or heat treatment. Such control enables spatial tuning of anisotropy and multifunctional properties within a single component. For electrical machines, this opens new possibilities to locally balance magnetic softness and electrical resistivity, reducing energy losses without added materials or complex architectures. More broadly, the study points toward a future where manufacturing strategies are used not only to shape components, but to embed functionality directly into their internal structure, supporting more efficient and sustainable energy technologies.

Introduction

Soft magnetic materials (SMMs) are essential components of electric motors, transformers, and various energy-conversion devices.[1,2] As electrification and renewable energy adoption accelerate globally, there is growing demand for high-power-density electric motors that are efficient, reliable, and sustainable.[3,4] The performance of SMM plays a critical role in minimizing energy losses and enabling efficient magnetic flux circulation in these systems.[5,6] Therefore, developing advanced SMMs tailored to evolving application requirements is crucial.[7,8]

A high-performance SMM typically possesses properties such as high magnetic permeability, low coercivity, high saturation magnetization, low magnetic loss, and high electrical resistivity, which are necessary to reduce eddy current losses caused by changing magnetic fields.[9,10] Common examples of SMM include iron–silicon alloys (electrical steels), iron–nickel alloys, iron–cobalt alloys, and soft magnetic composites.[10,11] Among these, iron–silicon alloys, particularly with 3 to 4 wt% Si in Fe are widely used in electrical machines due to their good balance of performance and manufacturability.[12,13] However, their use is largely limited to low frequency applications where core losses from eddy currents and hysteresis remains manageable.[14] For high-frequency, high-efficiency devices, there is a growing interest in high-silicon steel containing ~6.5 wt% Si. This composition offers key advantages, including high electrical resistivity, reduced iron loss, and near-zero magnetostriction and high saturation magnetization.[13,14] Despite these functional advantages, their use is limited by processing difficulties. The main issue is brittleness due to ordered phase formation,

Mukesh Murali, Department of Mechanical Engineering, Chalmers University of Technology, 41296 Gothenburg, Sweden;
Eduard Hryha, Department of Mechanical Engineering, Chalmers University of Technology, 41296 Gothenburg, Sweden;
Uta Klement, Department of Mechanical Engineering, Chalmers University of Technology, 41296 Gothenburg, Sweden;
Varun Chaudhary, Department of Mechanical Engineering, Chalmers University of Technology, 41296 Gothenburg, Sweden;
varunc@chalmers.se
*Corresponding author
doi:10.1557/s43577-026-01142-7

© The Author(s) 2026

which makes them unsuitable for conventional methods such as rolling or stamping.[15,16]

Additive manufacturing (AM) has proven to be an effective method for producing bulk high-silicon steel components, as the high cooling rates associated with the technique help alleviate the brittleness issue by suppressing the ordered phases.[11,16,17] However, optimizing AM process parameters remains a time-consuming process, as the solidification-driven microstructure is highly sensitive to process conditions, which in turn control the resulting properties.[18,19] To accelerate process optimization and microstructure–property correlation, high-throughput (HT) strategies are increasingly employed. AM is particularly well-suited for HT materials discovery, enabling the fabrication of samples with systematically varied compositions or process conditions within a single build.[20,21] When combined with other HT characterization tools, such approaches can significantly accelerate the development of multifunctional SMMs.

One of the key advantages of AM lies in its ability to tailor microstructures through control of process parameters.[22,23] Numerous studies have investigated the effects of energy input on the magnetic performance of Fe–Si alloys.[24,25] However, the role of laser path (scan rotation angle), a parameter that can significantly alter thermal gradients, grain morphology, and solidification behavior, remains unexplored. Understanding its influence on mechanical, electrical, and magnetic properties of Fe–6.5 wt% Si alloys is essential for advancing the design of high-performance soft magnetic components and exploiting the full potential of AM for functional materials.

In this work, an HT approach is employed to investigate the effect of laser path rotation on multi-properties of Fe–6.5 wt% Si steel processed by powder bed fusion-laser beam (PBF-LB). A single sample incorporating four scan rotation angles (0°, 45°, 67°, and 90°) is designed for HT characterization and structure–property correlation under identical processing conditions. The printed regions were systematically characterized for their grain morphology, crystallographic texture, magnetic performance, electrical resistivity, and hardness. This integrated approach provides new insight into how laser path engineering can be used to tune the microstructure and coupled properties of Fe–6.5 wt% Si steel, supporting site-specific design of soft magnetic components for advanced electrical systems.

Materials and methods

Materials

Pre-alloyed Fe–6.5 wt% Si gas-atomized powder (Höganäs AB, Sweden) was used as the feedstock for PBF-LB. The powder particles exhibited spherical morphology with smooth surface and a particle size distribution ranging from 10 to 45 µm. X-ray diffraction pattern confirmed the powder's single-phase body-centered cubic (bcc) structure. Energy-dispersive x-ray spectroscopy (EDS) confirmed the expected elemental composition, showing peaks corresponding only to Fe and Si, with no detectable impurities (**Figure S1** in Supplementary information).

Methods

PBF-LB experiments were conducted using an EOS M100 system (EOS GmbH, Germany), equipped with a Yb-fiber laser (maximum power of 200 W, ~40-µm spot size. The oxygen level was maintained below 1000 ppm, by purging the build chamber with argon gas. A systematic design of experiments (DoE) approach was employed to identify suitable processing parameters. The laser power and scan speed were varied from 90 to 170 W and 600 to 1400 mm/s, respectively, while maintaining a constant hatch distance of 0.06 mm and layer thickness of 0.02 mm. A total of 45 unique parameter combinations were screened using a high-throughput approach. Based on this screening, the selected parameters for the present study were 140 W laser power, 900 mm/s scan speed, 0.06 mm hatch distance, and 0.02 mm layer thickness.

Two cuboidal specimens were designed using Materialise Magics software, incorporating partitioned regions as illustrated in **Figure 1**a. The specimens had dimensions of $5 \times 5 \times 2$ mm for the vertical configuration and $5 \times 2 \times 5$ mm for the horizontal configuration. All structures were fabricated using a bidirectional laser scanning strategy, which involves alternating the scanning direction within each layer. In addition to this, the laser orientation was varied between layers according to four predefined rotation angles—0° (no rotation), 45°, 67°, and 90°—as illustrated in Figure 1b. A constant stripe width of 5 mm and a stripe overlap of 0.1 mm were maintained throughout the process. To facilitate a high-throughput methodology for sample preparation and subsequent characterization, all specimens were consolidated and printed as a single integrated build (Figure 1c). The samples were studied in as-printed and annealed conditions. They were annealed at 1150°C under argon atmosphere for 1 h using a 15°C/min ramp rate and followed by the furnace cooling.[26,27] Sections were taken parallel to both the build direction and scanning planes. Samples were hot mounted, ground using 500–2000 mesh SiC paper and polished using 3 µm and 1 µm diamond suspension. For EBSD analysis, a final fine polishing was performed using colloidal OP-S silica suspension.

Optical microscopy (OM) was performed using a Zeiss Axioscope 7 machine equipped with an automated stage enabling the stitching of images to capture whole cross-section images for calculating relative density. The obtained images were analyzed using ImageJ software. X-ray diffraction (XRD) was performed using SAXSLAB Mat: Nordic equipped with a Cu Kα source ($\lambda = 1.5406$ Å) facilitating automated sequential characterization of multiple samples through an integrated setup combining robotic sample handling, precise software-controlled positioning, and motorized stages. The pattern was collected over a 2θ range of 25° to 90° using a step size of 0.015° and a time per step of 1 s; and the data analysis were performed using the DIFFRAC.EVA software from Bruker. Gemini 450 Field Emission Scanning Electron Microscope (FEG-SEM) equipped with a Symmetry S3 EBSD detector (Oxford Instruments,

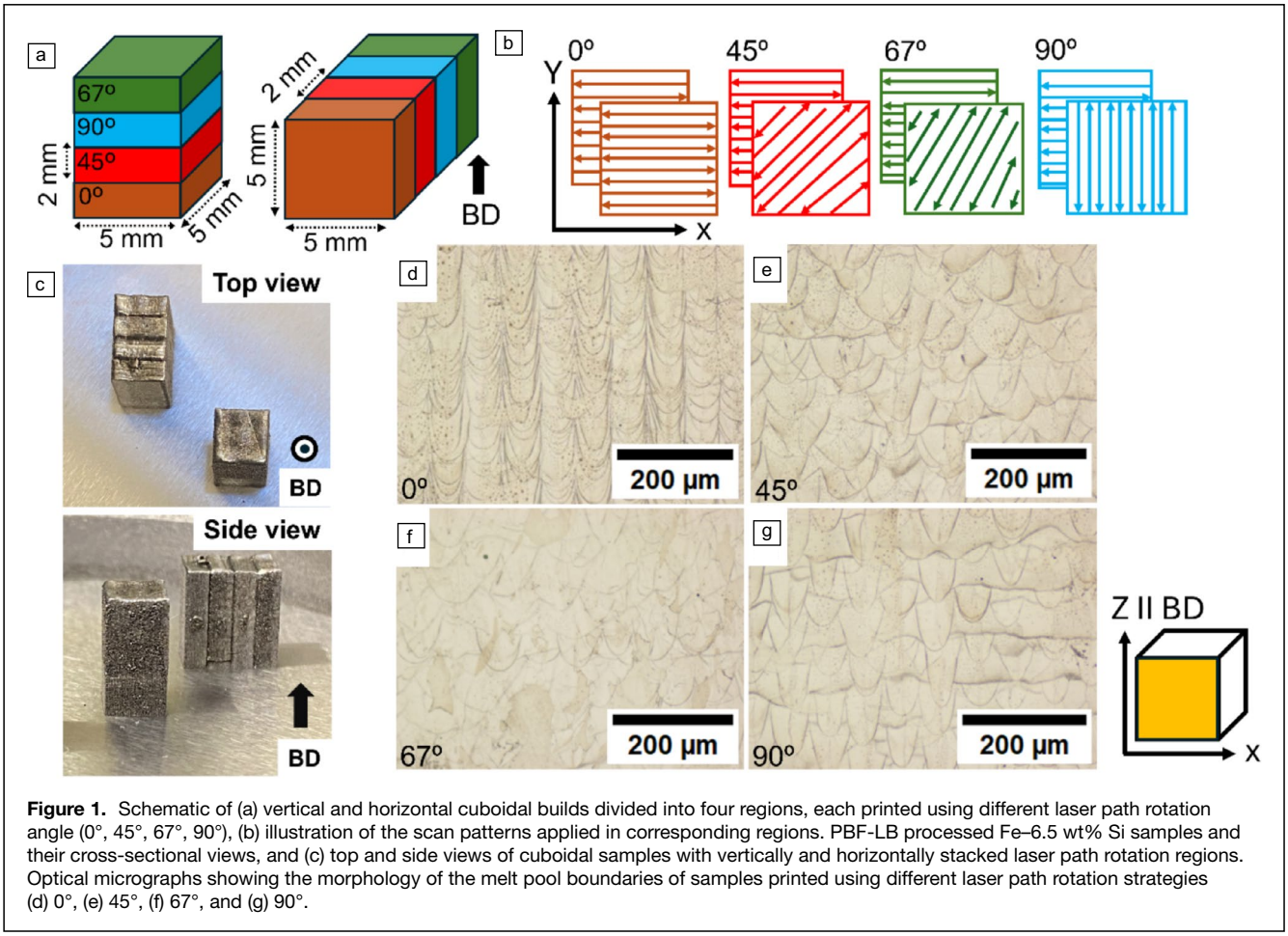

Figure 1. Schematic of (a) vertical and horizontal cuboidal builds divided into four regions, each printed using different laser path rotation angle (0°, 45°, 67°, 90°), (b) illustration of the scan patterns applied in corresponding regions. PBF-LB processed Fe–6.5 wt% Si samples and their cross-sectional views, and (c) top and side views of cuboidal samples with vertically and horizontally stacked laser path rotation regions. Optical micrographs showing the morphology of the melt pool boundaries of samples printed using different laser path rotation strategies (d) 0°, (e) 45°, (f) 67°, and (g) 90°.

Abingdon-on-Thames, UK) were used for microstructural studies. Large-area EBSD maps were obtained at 150 × magnification and a step size of 1 µm. The samples were tilted to 70° and an operating voltage of 20 kV and a working distance of around 18 mm were applied. The data analysis was performed using Aztec Crystal software.

To investigate the mechanical properties, Vickers hardness measurements were carried out using a Durascan-70 G5 hardness tester, which performs automated hardness tests and thus enables high-throughput approach in the characterization. All samples were tested at a force of HV1 (1 kgf) with a hold time of 10 s, and the images were taken at 20 × magnification. Ten readings were taken on each sample by randomly selecting the indentation points (as per ASTM standard) and the average were taken with standard deviations to obtain the hardness values. Electrical resistivity was measured using a CMT-SR2000N (Changmin Tech) 4-point probe setup. The measurements were performed by aligning the probes perpendicular to the build direction. The resistance values were obtained from the machine, and the resistivity values were calculated using the approach given in References 28, 29.

The magnetic measurements were performed using the Lake Shore Cryotronics 8600 series vibrating sample magnetometer (VSM). Small samples within the range of 10–25 mg were used for the measurements and to avoid the shape effect, cubic samples were used for the measurements. A magnetic field of ±1270 kA/m was used to obtain hysteresis curves. Magnetic properties such as intrinsic coercivity (H_c) and saturation magnetization (M_s) were measured by aligning the build direction in parallel (H ∥ BD) and perpendicular (H ⊥ BD) to the applied magnetic field. In this study, saturation magnetization refers to the magnetization measured at an applied field of 1270 kA/m. Mass magnetic susceptibility (χ_m) was calculated by taking the slope of the initial curve of the magnetization verses applied magnetic field (M–H) curves.

Results and discussion

Laser path influence on melt pool evolution

The Fe–6.5 wt% Si samples were successfully printed using the previously mentioned process parameters. Figure 1d–g presents optical micrographs of the etched samples, highlighting the melt pool morphology under different laser path rotation strategies. Although the hatch distance and layer thickness were kept constant, the shape, size and orientation of the melt pools vary significantly with the laser path rotation due to

changes in the remelting pattern across layers. In the 0° laser path rotation condition (Figure 1d), the melt pools are stacked vertically, aligned with each other, and penetrate deeper than the nominal layer thickness due to repeated remelting. In contrast, the 45° and 90° laser path rotations show more heterogeneous melt pool arrangements, due to re-melting on successive layers (Figure 1e and g). At a rotation angle of 67°, a completely randomized melt pool orientation is observed (Figure 1f). The change in the laser path rotation and thus the re-melting process in successive layers significantly influences the melt pool morphology and orientation, as evident from the images.

Grain morphology and crystallographic texture

To investigate grain morphology and crystallographic orientation, microstructural analysis was performed on both as-printed and annealed samples. A high-throughput approach was implemented by using large-area EBSD mapping, allowing acquisition of the entire region of interest in a single scan. These comprehensive maps were then examined in discrete sections for detailed structure–property correlation. The large-area EBSD maps in inverse pole figure (IPF) coloring are shown in **Figure 2**a. Sectioned maps for different samples are presented in Figure 2b–e (as-printed, *XZ* cross-section), Figure 2f–i (as-printed, *XY* cross-section). The corresponding pole figures are provided in **Figures S2 and S3** (Supplementary information).

Across all laser path rotations, the as-printed samples exhibit elongated columnar grains aligned along the build direction (Figure 2a), consistent with directional solidification and epitaxial grain growth driven by the thermal gradient along the build axis.[30,31] However, the degree of grain alignment and crystallographic texture varies with laser path rotation. For 0° and 90° laser path rotations, the grains maintain a stable columnar morphology across layers (Figure 2b, e), but their crystallographic textures differ significantly. The 90° rotation develops a dominant ⟨001⟩ texture parallel to the build direction (Figure 2e), whereas the 0° sample exhibits a comparatively weaker texture (Figure 2b). Quantitative pole figure analysis further confirms this difference, with the texture intensity—expressed in multiples of random distribution (MRD)—increases from 4.56 MRD for the 0° rotation to 11.85 MRD for the 90° rotation (Figure S2, Supplementary information).

In contrast, the 45° and 67° rotation angles produce more heterogeneous microstructures with weaker textures (Figure 2c–d), exhibiting texture intensities of 4.40 MRD and 5.17 MRD, respectively (Figure S2). The continuously changing melt pool orientation disturbs stable growth,[32] leading to variable grain widths and measurable intragranular misorientation gradients. These gradients appear as color variations within the individual grains and indicate the presence of residual stresses induced by the rapid thermal cycles during the laser melting process.[31,33]

The *XY* sections further highlight the effect of rotation angle on grain arrangement. At 0°, narrow band like grains appear parallel to the scan direction (Figure 2f), whereas the 90° rotation yields a more square-like grain pattern due to periodic perpendicular remelting (Figure 2i). The spread of the red color indicates the orientation of grains along ⟨001⟩ indicating a stronger texture compared to other samples. The 45° and 67° rotations again show irregular grain shapes and weak or absent texture (Figure 2g–h), consistent with their more variable melt pool geometry.

Average grain area values and grain diameters are calculated for each case from the EBSD maps and are summarized in **Table SI** (Supplementary information). Grain structures were characterized by applying a grain-boundary misorientation threshold of 10°. For each specimen, the grain size was quantified on both the build direction (*XZ*) and top (*XY*) surfaces, and area-weighted mean values over the fitted ellipse major/minor diameter were used to obtain representative values. Since the grains in these samples are elongated and columnar, the area-weighted mean fitted ellipse diameter, and area provides a more meaningful descriptor than conventional grain size. The conventional method assumes a nearly equiaxed grain, which is not appropriate for anisotropic grain morphologies observed here.[34]

Among the *XZ* sections (along BD), the samples printed with 90° laser path rotation produced the largest columnar grains with an area-weighted mean area of 11,974 ± 1952 μm^2, followed by the 67°, 45° and 0° rotations, which yielded average area of 6974 ± 2176, 6254 ± 2003, and 5024 ± 1952 μm^2, respectively (Table SI, Supplementary information). On the *XY* surface (perpendicular to BD), the sample prepared with 90° laser path rotation again showed the largest area-weighted mean area (4975 ± 1639 μm^2). The 45° and 67° samples exhibited similar average grain area (2729 ± 1074 and 2893 ± 1 018 μm^2), reflecting their mixed grain-size distributions, whereas the sample with no laser path rotation (0°) has the narrowest grains, and with an area of 1939 ± 805 μm^2.

Analysis based on fitted ellipse major and minor diameters shows that the 0° rotation exhibits the highest aspect ratio (3.7), while the 90°, 45°, and 67° rotations show similar aspect ratios of 2.9, 2.9, and 2.8, respectively (Table SI, Supplementary information). Although all conditions produce columnar grains, this indicates that the 0° rotation leads to narrower columnar grains when viewed on the *XY* plane, whereas the 90° rotation produces coarser columnar grains with larger cross-sectional widths. The 45° and 67° rotations result in columnar grains with moderate widths and more heterogeneous size distributions.

Overall, the 90° rotation produces a coarser columnar microstructure with the strongest ⟨001⟩ texture, whereas the 0° rotation results in narrower columnar grains with a higher grain boundary density. Since, the ⟨001⟩ direction corresponds to the easy magnetization axis in Fe–Si alloys, facilitating domain wall motion and enhancing magnetic response which is beneficial for soft magnetic performance.[13,14] The 45° and 67° rotations lead to more heterogeneous microstructures with comparatively weaker textures. These findings indicate that

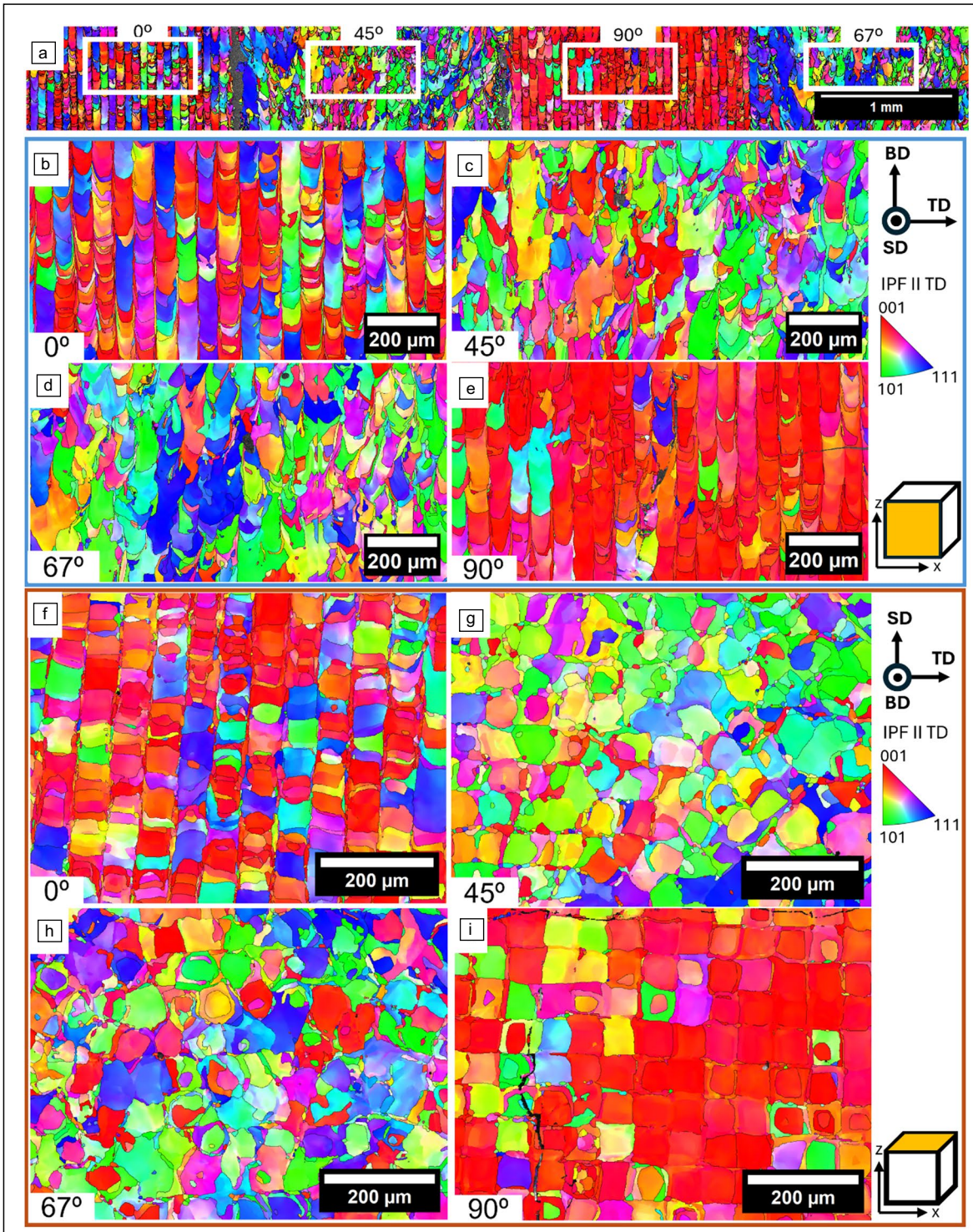

Figure 2. EBSD orientation maps (IPF coloring) of the *XZ* (parallel to BD) and *XY* (perpendicular to BD) cross-sections for as-printed Fe–6.5 wt% Si samples. (a) Large-area map of the entire sample showing regions corresponding to different laser path rotations. *XZ* cross-sections for scan rotation strategies are shown in the blue box: (b) 0°, (c) 45°, (d) 67°, and (e) 90°; *XY* cross-sections for scan rotation strategies are shown in the red box: (f) 0°, (g) 45°, (h) 67°, and (i) 90°. The IPF color key and analyzed surface are valid for all maps. BD, build direction; SD, scanning direction; TD transverse direction.

both grain size and morphology are strongly influenced by the laser path rotation angle.

After annealing the samples at 1150°C, recrystallization and grain growth produced substantially coarser grains as shown in **Figure 3**. All EBSD maps were taken from the *XZ* cross section of the samples and corresponding pole figures of the maps are provided in **Figure S4** (Supplementary information). Although all samples are annealed under identical conditions, they exhibit different degrees of recrystallization and grain growth. The 0° and 45° rotation samples (Figure 3a–b) exhibit extensive grain growth and are mostly free of in-grain misorientations, indicating effective stress relief. Conversely, samples processed with 67° and 90° laser path rotations (Figure 3c–d) display only partial recrystallization, resulting in heterogeneous microstructures composed of coarse grains interspersed with finer ones.

The remaining in-grain misorientations indicate incomplete stress relaxation. Such variation in recrystallization behavior, despite identical heat treatment, is consistent with earlier reports for Fe–6.5 wt% Si[26] and likely reflects differences in stored energy and melt pool geometry associated with each scan rotation. Extended annealing (holding the samples for a longer duration at the same annealing temperature) can facilitate a higher degree of recrystallization and subsequent grain growth. Due to the limited number of grains captured in the EBSD maps, a reliable assessment of crystallographic texture could not be made from EBSD alone. The corresponding PF maps are provided in the Supplementary information (Figure S4). Therefore, the texture evaluation of the annealed samples is performed based on XRD analysis using the Harris method, with the corresponding texture coefficients presented in the following section.

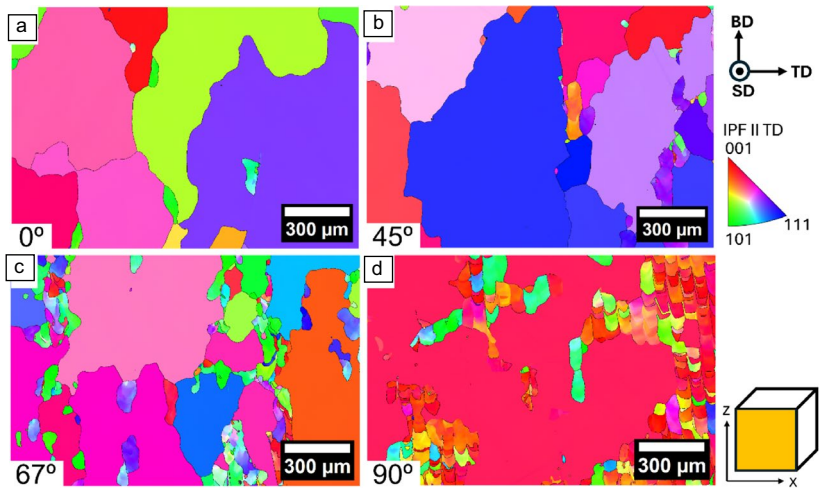

Figure 3. EBSD orientation maps (IPF coloring) of the *XZ* cross-section (parallel to BD) for annealed Fe–6.5 wt% Si samples printed with the scan rotation strategies. (a) 0°, (b) 45°, (c) 67°, and (d) 90°. The IPF color key and analyzed surface are valid for all maps. BD, build direction; SD scanning direction; TD transverse direction.

Phase evolution and preferred orientation analysis by XRD

High-throughput XRD measurements were carried out on both the as-printed and annealed samples to understand the crystal structure information, e.g., present phase(s) and any preferred orientation. The x-ray beam was selectively focused on specific areas by controlling its size. By rotating the detector and sample relative to the beam, diffraction patterns were collected over the 2θ range of 25° to 90° (**Figure 4**).

For the as-printed and annealed samples, the XRD patterns contain bcc diffraction peaks expected for the disordered α-FeSi phase (Figure 4a–b). No ordered phases such as D03 or B2 were detected, even though they are normally present in Fe–Si alloys with > 5 wt% Si.[35] This absence of ordered phases (**Figure S5**, Supplementary information) can be explained by the very high cooling rates during PBF-LB,[15,25] typically on the order of 10^4–10^6 K/s,[36] which are several orders of magnitude higher than for conventional casting (~10^0–10^2 K/s).[37] The detection limits of laboratory XRD may also contribute to the lack of observable ordering.

The relative intensities (I) of the 110 and 200 reflections also provide a qualitative indication of preferred orientation in the samples. The $I(200)/I(110)$ ratio is higher for the 0° and 90° laser path rotations (0.24 and 0.40, respectively) than for the 45° and 67° cases (0.06 and 0.16, respectively), suggesting a stronger ⟨001⟩-type orientation component in these samples. This trend is consistent with the EBSD observations, where the 90° sample shows a clear ⟨001⟩ fiber texture and the 45° and 67° samples exhibit more random orientations. This observation is further supported by the texture coefficient (TC) values calculated using the Harris texture index equation,[38,39] as listed in **Table SII** (Supplementary information). The higher TC values for the (200) reflection in the 90° sample—both in the as-printed and annealed states—indicate a strong ⟨001⟩ texture. In contrast, the sample without laser path rotation (0°) exhibits a strong ⟨100⟩-type orientation after annealing, as evidenced by its increased TC compared to the nearly random orientation observed in the as-printed condition.

Magnetic properties and anisotropy

To understand the influence of laser path rotation on the magnetic properties, magnetic hysteresis measurements were performed on the as-printed and annealed samples with the applied field oriented parallel and perpendicular to the build direction (BD). The M–H curves for the as-printed samples (**Figure 5**a) show a

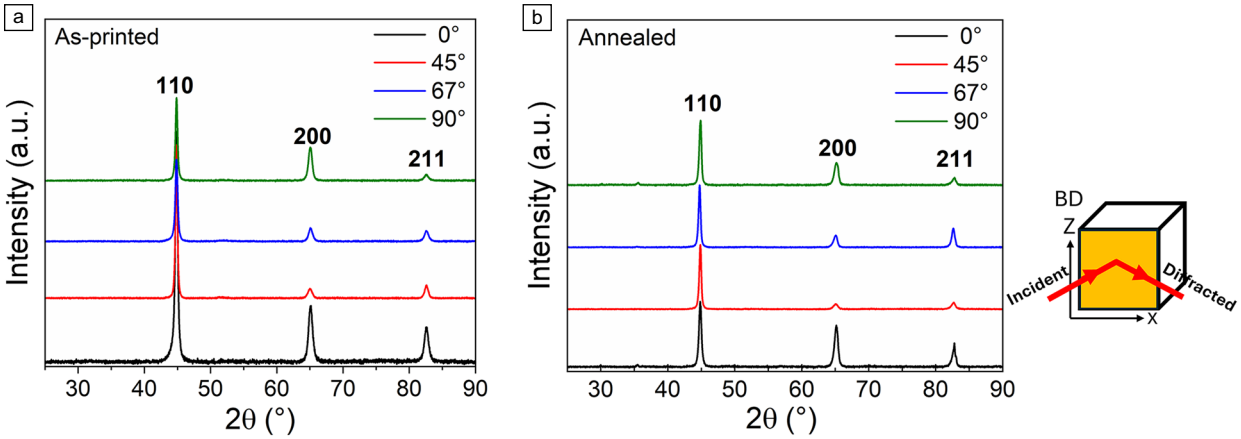

Figure 4. XRD patterns of (a) as-printed and (b) annealed samples printed with different scan rotation angles.

strong dependence of magnetic response on the laser path rotation, despite all samples being fabricated under identical alloy composition and process energy.

As-printed condition

Under magnetic field parallel to build direction (H ∥ BD) condition, the samples approach magnetic saturation more readily than under magnetic field perpendicular to build direction (H ⊥ BD) (Figure 5b), reflecting the anisotropic columnar grain structure generated during PBF-LB processing. Among the laser path rotation conditions, the 90° rotation sample exhibits the lowest coercivity (81.4 A/m) and the highest saturation magnetization (197.2 A m^2/kg) at the maximum applied field. The 67° rotation sample shows the highest susceptibility (11.9×10^{-4} m^3/kg), followed by the 90°, 45° and 0° rotation samples, with χ_m values of 11.2×10^{-4}, 9.7×10^{-4} and 7.7×10^{-4} m^3/kg, respectively. Thus, the 90° rotation condition optimizes low coercivity and high magnetization, whereas the 67° rotation condition yields the largest initial susceptibility (Figure 5c–d). These trends correlate with the observed microstructural features; however, the underlying magnetic behavior is influenced by multiple interacting factors rather than a single mechanism.[14] In the as-printed condition, the 90° rotation sample exhibits the lowest coercivity and one of the highest susceptibility values, which can be associated with its coarser grains and stronger ⟨001⟩ texture. In contrast, the narrower columnar grains observed in the 0° rotation sample may contribute to increased resistance to domain wall motion due to the higher grain-boundary density. The 45° and 67° rotation samples exhibit intermediate magnetic behavior consistent with their mixed columnar morphologies. Although the magnetic response generally follows the observed variations in texture intensity and grain morphology, the behavior is also influenced by other factors, such as residual stresses, and local microstructural heterogeneity.[14,40]

When the field is applied perpendicular to BD (H ⊥ BD), the magnetization at the maximum applied field decreases for all samples and the coercivity increases by approximately a factor of two (**Table I**). This behavior arises because in the H ⊥ BD orientation, the magnetization path intersects a larger number of grain boundaries, which increases the domain wall pinning and delays the reaching of saturation. The influence of laser path rotation is therefore less pronounced in this orientation, as the response is dominated by grain-boundary density. The maximum magnetic field used in this study (~1270 kA/m) is also insufficient to fully saturate the material under H ⊥ BD.

Overall, better soft magnetic properties are obtained when the samples are measured along the BD (H ∥ BD). The anisotropic response originates from the elongated columnar grains formed during solidification, which introduce substantially fewer pinning sites when the field is applied parallel to BD, enabling easier domain wall motion and improved magnetic performance.[31,41] The microstructural variations induced by the laser path rotation influence the response through a combination of grain size, crystallographic texture, and grain-boundary characteristics: the 0° rotation sample, with narrower and randomly oriented grains, exhibits higher coercivity, whereas the 90° rotation sample, characterized by coarser grains and a stronger ⟨001⟩ texture, shows reduced coercivity and improved magnetic response. The 45° and 67° rotation samples fall between these two extremes due to their more irregular columnar morphologies.

Annealed condition

Annealing substantially altered the magnetic response of the samples and reduced the anisotropy observed in as-printed condition. The *M*–*H* curve of the annealed samples (Figure 5e) together with magnified regions in Figure 5f, h shows that the difference between measurements performed along and perpendicular to the build direction becomes markedly smaller after heat treatment. The M_s, H_c and χ_m values obtained for different laser path rotations on both measurement conditions (H ∥ BD and H ⊥ BD) are given in Table I. Coercivity decreases for all laser path rotation conditions. The 0° rotation sample exhibits the largest reduction, with H_c decreasing from

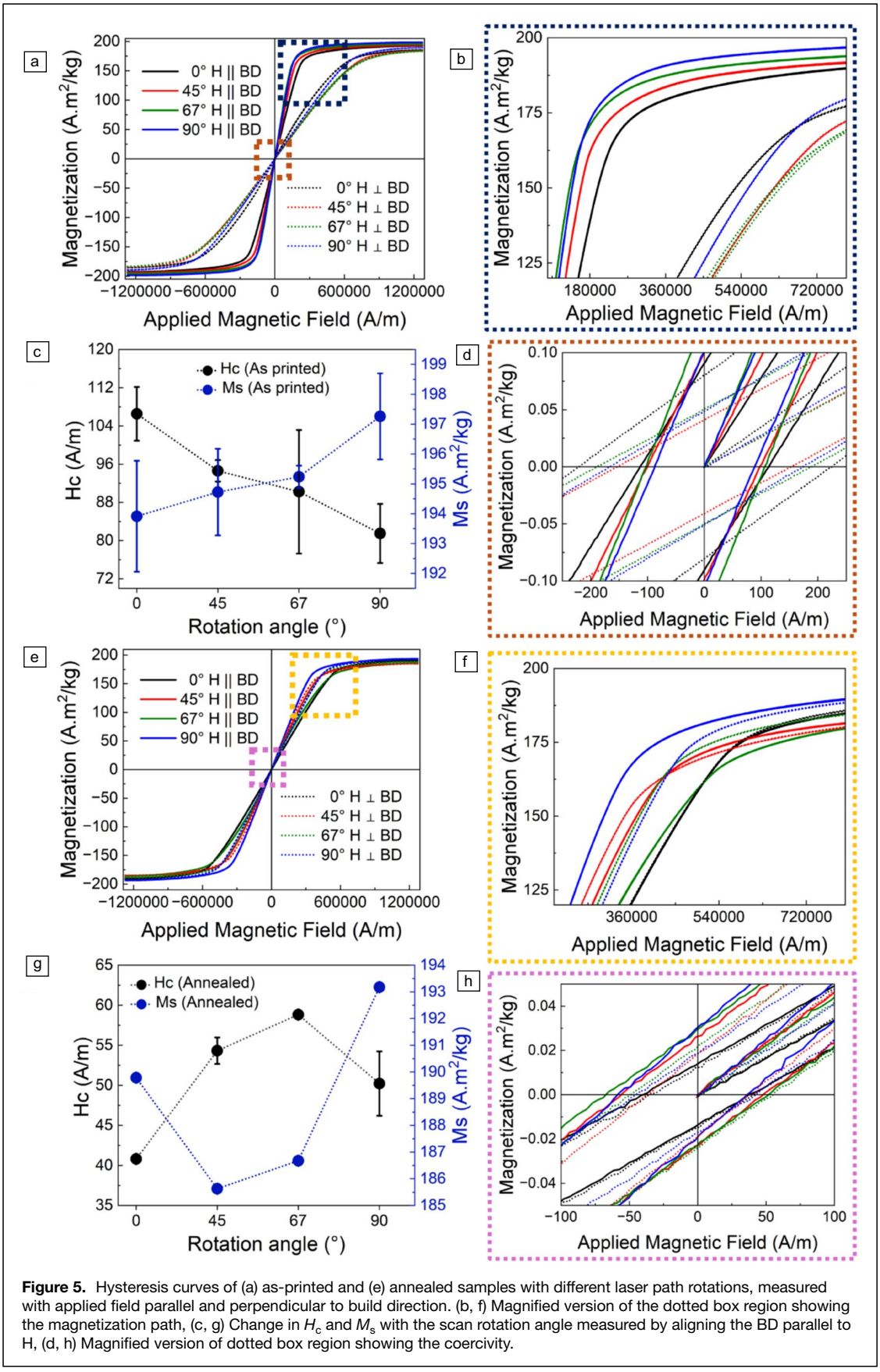

Figure 5. Hysteresis curves of (a) as-printed and (e) annealed samples with different laser path rotations, measured with applied field parallel and perpendicular to build direction. (b, f) Magnified version of the dotted box region showing the magnetization path, (c, g) Change in H_c and M_s with the scan rotation angle measured by aligning the BD parallel to H, (d, h) Magnified version of dotted box region showing the coercivity.

106.6 to 39.9 A/m under H ∥ BD and from 220.8 to 34.9 A/m under H ⊥ BD. For the 45°, 67°, and 90° rotation samples, coercivity decreases by roughly 1.5–3.5 times depending on the measurement orientation. In contrast, changes in magnetization at the maximum applied field are relatively modest. Consistent with the as-printed condition, the annealed samples retain the same ordering of saturation magnetization (Figure 5g), with the 90° rotation sample exhibiting the highest M_s (193.1 A m^2/kg under H ∥ BD) and the 45° rotation sample the lowest (184.8 A m^2/kg under H ⊥ BD). This indicates that, although annealing reduces the overall anisotropy, the crystallographic texture is not entirely eliminated. Residual microstructural features, including incomplete randomization of crystallographic orientation, grain size distribution, and local heterogeneities, associated with the laser path rotation continue to influence the magnetic response.

The susceptibility (χ_m) also becomes far less direction-dependent after annealing. In the annealed condition, χ_m decreases under H ∥ BD and increases under H ⊥ BD compared with the as-printed condition for all laser path rotation conditions. This behavior is attributed to the reduction of microstructural anisotropy after annealing, which decreases the preferential magnetization along the build direction and facilitates domain wall motion under H ⊥ BD, leading to a more isotropic magnetic response. This reduction in magnetic anisotropy is consistent with the microstructural evolution observed after annealing: grain growth reduces the density of grain boundaries, decreasing the number of domain wall pinning sites and improving the soft magnetic response.[42] The disappearance of in-grain misorientations (Figure 3) indicates substantial residual-stress relief.[31] These combined effects lower coercivity and reduce the sensitivity of the magnetic response to measurement orientation.

Overall, the annealed samples display a homogenized and nearly isotropic magnetic response, in contrast to the strong directional and laser path dependent behavior observed in the as-printed condition. These results confirm that high temperature annealing is highly effective in mitigating microstructural anisotropy and stabilizing the magnetic performance of PBF-LB processed Fe–6.5 wt% Si alloys.

Mechanical and electrical properties

The mechanical properties were investigated by conducting Vickers micro-hardness measurements on cross-sections parallel to the build direction on both as-printed and annealed samples. Average hardness values along with their standard deviations are presented in **Figure 6**a. In the as-printed condition, the sample printed without laser rotation (0°) exhibited

Table I. Summary of the magnetic properties of the as-printed and annealed Fe-6.5 wt%Si samples measured by aligning the build direction parallel (∥) and perpendicular (⊥) to the applied magnetic field.

Laser path rotation (°) and condition	Sample orientation w.r.t. applied magnetic field	Coercivity, H_c (A/m)	Saturation magnetization, M_s (A m^2/kg)	Mass magnetic susceptibility, χ_m (m^3/kg)	References
As-printed					
0	H ∥ BD	106.6	193.9	7.7×10^{-4}	This work
	H ⊥ BD	220.8	185.1	3.4×10^{-4}	
45	H ∥ BD	94.6	194.7	9.7×10^{-4}	
	H ⊥ BD	153.4	183.9	2.6×10^{-4}	
67	H ∥ BD	90.2	195.2	11.9×10^{-4}	
	H ⊥ BD	189.3	182.9	2.6×10^{-4}	
90	H ∥ BD	81.4	197.2	11.2×10^{-4}	
	H ⊥ BD	167.2	189.1	2.8×10^{-4}	
90	H ∥ BD	165	197	8.6×10^{-4}	31
	H ⊥ BD	178	188	5.1×10^{-4}	
90	–	78	–	–	43
	–	205	–	–	44
Annealed at 1150°C					
0	H ∥ BD	39.9	189.7	3.4×10^{-4}	This work
	H ⊥ BD	34.9	190.6	3.5×10^{-4}	
45	H ∥ BD	55.7	185.6	4.5×10^{-4}	
	H ⊥ BD	37.1	184.8	4.8×10^{-4}	
67	H ∥ BD	67	186.6	4.3×10^{-4}	
	H ⊥ BD	48.8	188.4	4.3×10^{-4}	
90	H ∥ BD	58.5	193.1	5.1×10^{-4}	
	H ⊥ BD	45.2	192.9	4.0×10^{-4}	
90	H ∥ BD	90	193	6.5×10^{-4}	31
	H ⊥ BD	90	191	6.0×10^{-4}	

The magnetic properties reported for PBF-LB processed Fe–6.5 wt% Si alloys in previous studies are also included for comparison.

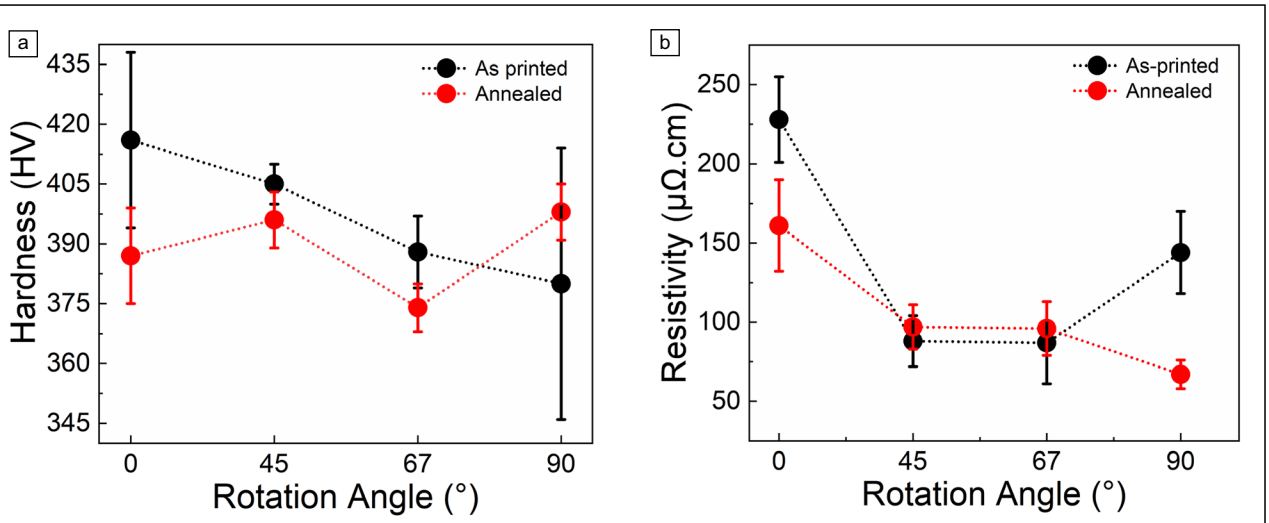

Figure 6. (a) Vickers hardness of the as-printed and annealed samples printed with different scan rotation strategies. (b) Electrical resistivity of the as-printed and annealed samples printed with different laser path rotations.

the highest hardness (416 HV). The samples with laser path rotations of 45°, 67°, and 90° showed hardness values of 405, 388, and 380 HV, respectively. After annealing, the hardness values decreased for the 0°, 45°, and 67° rotation samples (387, 396, and 374, respectively), whereas the 90° rotation sample showed a slight increase (398 HV).

These trends can be understood from the grain structures. According to Hall–Petch equation, hardness is inversely proportional to the square root of the grain diameter.[45,46] The higher hardness observed in the as-printed 0° sample can be attributed to its narrow columnar grains and increased grain boundary density (Figure 2b, f), which restrict dislocation motion and reduce plastic deformation.[47,48] In contrast, the 90° rotation sample contains coarser, cuboidal shape columnar grains (Figure 2e and i) reflected in its lower hardness. The 45° and 67° rotation samples have more mixed grain sizes and shapes, giving intermediate hardness values. After annealing, the reduction in hardness for the 0°, 45°, and 67° samples follows the recrystallization and grain growth seen in Figure 3. The slight increase in hardness for the 90° sample is likely due to the bimodal microstructure (Figure 3d), where finer grains remain between coarsened regions.

Electrical resistivity was measured on the *XZ* cross-sections (parallel to the build direction) using a four-point probe method (Figure 6b). In the as-printed condition, the 0° rotation sample showed the highest resistivity (228 μΩ·cm), while the 45°, 67°, and 90° samples exhibited values of 88, 87, and 144 μΩ·cm, respectively. After annealing, the resistivities changed to 161 μΩ·cm (0°), 97 μΩ·cm (45°), 96 μΩ·cm (67°), and 67 μΩ·cm (90°).

The exceptionally high resistivity of the 0° rotation sample in the as-printed condition can be primarily attributed to its narrow columnar grains and the associated high density of grain boundaries, which act as effective electron scattering centers.[49,50] The mixed grain structures in the 45° and 67° samples result in resistivity values close to the reported value of ~82 μΩ·cm for Fe–6.5 wt% Si.[13,14] In contrast, the relatively high resistivity observed in the 90° rotation sample, despite its larger grain size, indicates that factors beyond grain boundary density also contribute. In this case, the strong ⟨001⟩ texture, columnar grain morphology, and the orientation of grain boundaries with respect to the measurement direction can introduce electron scattering.[51] Furthermore, residual stresses and microstructural heterogeneities inherent to the PBF-LB process may additionally influence resistivity. This highlights that electrical resistivity in these samples is governed by a combination of grain-boundary characteristics, crystallographic texture, and processing-induced microstructural features rather than grain size alone.

After annealing, both the 0° and 90° rotation samples show a clear reduction in resistivity, consistent with reduced electron scattering due to grain growth and a decrease in microstructural anisotropy. In contrast, the slight increase observed for the 45° and 67° rotation samples falls within the standard deviation. Although grain growth occurs in these cases, the microstructures remain heterogeneous after annealing, and changes in grain-boundary character and orientation can offset the expected reduction in scattering.

Overall, the ability to achieve both exceptionally high resistivity in some cases and a broad tunability of hardness and resistivity across scan rotations highlights the potential of PBF-LB to tailor Fe–6.5 wt% Si for multi-property applications, where reduced eddy current losses and adequate mechanical strength are essential.

All these findings demonstrate that the mechanical, electrical, and magnetic properties of PBF-LB fabricated Fe–6.5 wt% Si soft magnetic alloys are strongly dependent on the laser path rotation. Modifying the rotation angle provides a means of tailoring grain morphology, texture and grain boundary density, thereby enabling tunability of both functional

and structural performance. In this work, samples produced without laser path rotation showed increased electrical resistivity, which is very important for controlling eddy current losses, as well as balanced magnetic and mechanical behavior, and remained stable after annealing. On the other hand, the 90° rotation sample yielded superior magnetic properties while maintaining satisfactory electrical and mechanical characteristics. This process flexibility offers the potential for manufacturing Fe–Si components with spatially varying microstructure. For example, alternating layers with different microstructures could be tailored so that certain layers are optimized for optimal magnetic properties and others for increased electrical resistivity. This allows the material to act as its own insulating layer, eliminating the need for separate non-magnetic interlayers, improving both magnetic performance and component compactness. Compared to specialized route such as chemical-vapor-deposition used for high-silicon steels, this approach offers a simpler pathway with improved material efficiency and recyclability.

Conclusion

Laser path rotation was found to strongly influence melt pool geometry, grain morphology and the resulting mechanical, electrical and magnetic behavior of PBF-LB processed Fe–6.5 wt% Si. Narrow columnar grains formed when using no laser path rotation (0°) promoted higher resistivity, reflecting the increased grain-boundary density, while coarser and better aligned grains produced with 90° laser path rotation increased the soft magnetic properties. As printed samples exhibited pronounced magnetic anisotropy due to the elongated grain structure along the build direction. Annealing reduced this anisotropy through grain growth and stress relief, leading to a more uniform magnetic response across rotation conditions. Notably, coercivity values near 35 A/m were achieved after annealing. Reaching such low coercivity along with high resistivity in additively manufactured Fe–6.5 wt% Si represents a significant improvement, as this composition is difficult to process by conventional routes due to its intrinsic brittleness and strong ordering tendencies. The findings underline the central role of grain size, grain-boundary density and crystallographic alignment in governing the magnetic and electrical behavior of high-silicon steels. Laser path rotation therefore provides a practical route for tuning the balance between soft magnetic performance and resistivity, enabling the design of additively manufactured Fe–Si components with tailored microstructures and application specific functionality.

Acknowledgments

The authors acknowledge financial support from the Areas of Advance (AoA) in Production and Materials Science at Chalmers University of Technology. Authors acknowledge the Center for Additive Manufacture-Metal (CAM^2), supported by the Swedish Governmental Agency for Innovation Systems (Vinnova). Höganäs AB is acknowledged for providing the powders.

Funding

Open access funding provided by Chalmers University of Technology.

Data availability

Data produced for this manuscript are available upon reasonable request to the corresponding author.

Conflict of interest

On behalf of all authors, the corresponding author states that there is no conflict of interest.

Supplementary information

The online version contains supplementary material available at https://doi.org/10.1557/s43577-026-01142-7.

Open Access

This article is licensed under a Creative Commons Attribution 4.0 International License, which permits use, sharing, adaptation, distribution and reproduction in any medium or format, as long as you give appropriate credit to the original author(s) and the source, provide a link to the Creative Commons licence, and indicate if changes were made. The images or other third party material in this article are included in the article's Creative Commons licence, unless indicated otherwise in a credit line to the material. If material is not included in the article's Creative Commons licence and your intended use is not permitted by statutory regulation or exceeds the permitted use, you will need to obtain permission directly from the copyright holder. To view a copy of this licence, visit http://creativecommons.org/licenses/by/4.0/.

References

1. J.M. Silveyra, E. Ferrara, D.L. Huber, T.C. Monson, *Science* **362**, eaao0195 (2018)
2. L. Han, F. Maccari, I.R. Souza Filho, N.J. Peter, Y. Wei, B. Gault, O. Gutfleisch, Z. Li, D. Raabe, *Nature* **608**, 310 (2022)
3. Y. Guo, L. Liu, X. Ba, H. Lu, G. Lei, W. Yin, J. Zhu, *World Electr. Veh. J.* **14**(4), 114 (2023)
4. O. Gutfleisch, M.A. Willard, E. Brück, C.H. Chen, S.G. Sankar, J.P. Liu, *Adv. Mater.* **23**, 821 (2011)
5. H. Li, Y. Li, R. Zhao, S. Bandaru, Z. Zhang, H. Pan, J. Lin, Z. Liu, X. Liu, C. Hu, P. Guan, A. Pan, E. Zhang, Z. Li, H. Rong, X. Zhang, *Nat. Commun.* **16**, 9563 (2025)
6. L. Han, F. Maccari, I. Soldatov, N.J. Peter, I.R. Souza Filho, R. Schäfer, O. Gutfleish, Z. Li, D. Raabe, *Nat. Commun.* **14**, 8176 (2023)
7. J.M. Silveyra, A.M. Leary, V. DeGeorge, S. Simizu, M.E. McHenry, *J. Appl. Phys.* **115**, 17A319 (2014)
8. S.K. Sarkar, N. Keskar, L.P. Tan, T. Ingale, A. Chesetti, S. Dasari, K.P. Davidson, V. Chaudhary, N. Dahotre, R.V. Ramanujan, R. Banerjee, *Nat. Commun.* **17**, 2890 (2026)
9. B.R. Rodriguez-Vargas, G. Stornelli, P. Folgarait, M.R. Ridolfi, A.F. Miranda Pérez, A. Di Schino, *Materials* **16**(16), 5610 (2023)
10. K.I. Arai, K. Ishiyama, *J. Magn. Magn. Mater.* **133**, 233 (1994)
11. V. Chaudhary, S.A. Mantri, R.V. Ramanujan, R. Banerjee, *Prog. Mater. Sci.* **114**, 100688 (2020)
12. T.N. Lamichhane, L. Sethuraman, A. Dalagan, H. Wang, J. Keller, M.P. Paranthaman, *Mater. Today Phys.* **15**, 100255 (2020)
13. G. Ouyang, X. Chen, Y. Liang, C. Macziewski, J. Cui, *J. Magn. Magn. Mater.* **481**, 234 (2019)
14. R.M. Bozorth, *Ferromagnetism* (IEEE Press, New York, 1993), p.1
15. D. Xuan, C. Zhou, Y. Zhou, T. Jiang, W. Fan, Y. Mao, *J. Magn. Magn. Mater.* **571**, 170550 (2023)
16. B. Viala, J. Degauque, M. Fagot, M. Baricco, E. Ferrara, F. Fiorillo, *Mater. Sci. Eng. A* **212**, 62 (1996)
17. M. Garibaldi, I. Ashcroft, M. Simonelli, R. Hague, *Acta Mater.* **110**, 207 (2016)

18. H.S. Jang, S.H. Kim, G.-W. Park, J.B. Jeon, D. Kim, D. Kim, W.R. Kim, Y.S. Choi, S. Shin, *Materials* **16**, 7626 (2023)
19. M. Ji, H.-J. Shim, J.H. Kim, Y.-S. Lee, J.P. Choi, Y.-I. Lee, *Powder Metall.* **66**, 602 (2023)
20. W.H. Teh, V. Chaudhary, S. Chen, S.H. Lim, F. Wei, J.Y. Lee et al., *Addit. Manuf.* **58**, 102983 (2022)
21. S. Sheikh, B. Vela, P. Honarmandi, P. Morcos, D. Shoukr, A.M. Kotb, I. Karaman, A. Elwany, R. Arróyave, *NPJ Comput. Mater.* **11**, 179 (2025)
22. S. Gao, Z. Li, S. Van Petegem, J. Ge, S. Goel, J.V. Vas, V. Luzin, Z. Hu, H.L. Seet, D.F. Sanchez, H. Van Swygenhoven, H. Gao, M. Seita, *Nat. Commun.* **14**, 6752 (2023)
23. P. Köhnen, M. Létang, M. Voshage, J.H. Schleifenbaum, C. Haase, *Addit. Manuf.* **30**, 100914 (2019)
24. M. Zaied, A. Ospina-Vargas, N. Buiron, J. Favergeon, N.-E. Fenineche, *IEEE Trans. Magn.* **58**, 1 (2022)
25. M. Garibaldi, I. Ashcroft, N. Hillier, S. Harmon, R. Hague, *Mater. Charact.* **143**, 144 (2018)
26. M. Garibaldi, I. Ashcroft, J.N. Lemke, M. Simonelli, R. Hague, *Scr. Mater.* **142**, 121 (2018)
27. A. Di Schino, R. Montanari, M. Sgambetterra, G. Stornelli, A. Varone, G. Zucca, *J. Mater. Res. Technol.* **26**, 8406 (2023)
28. L.P. Tan, S.P. Padhy, Z. Tsakadze, V. Chaudhary, R.V. Ramanujan, *J. Mater. Res. Technol.* **20**, 4186 (2022)
29. L.P. Tan, V. Chaudhary, Z. Tsakadze, R. Ramanujan, *Sci. Rep.* **12**, 9504 (2022)
30. A. Leicht, C.H. Yu, V. Luzin, U. Klement, E. Hryha, *Mater. Charact.* **163**, 110309 (2020)
31. A.Z. Macknojia, J.V. Tran, M.P. Mckinstry, J. Galindo, Y. Jin, S. Dowden, S.M. Patil, M.V. Pantawane, K.V. Mani Krishna, R. Banerjee, S.S. Joshi, N.B. Dahotre, *Mater. Des.* **241**, 112883 (2024)
32. S.-H. Sun, K. Hagihara, T. Nakano, *Mater. Des.* **140**, 307 (2018)
33. A. Lodh, T.N. Tak, A. Prakash, P. Guruprasad, S.M. Keralavarma, A.A. Benzerga, C. Hutchinson, I. Samajdar, *Metall. Mater. Trans. A* **50**, 5038 (2019)
34. L. Chechik, A.D. Goodall, K.A. Christofidou, I. Todd, *Sci. Rep.* **13**, 10003 (2023)
35. F. González, Y. Houbaert, *Rev. Met.* **49**, 178 (2013)
36. K. Kosiba, T. Gustmann, J.T. Kim, J. Seok, J. Jung, L. Beyer et al., *J. Alloys Compd.* **967**, 171773 (2023)
37. S. David, J. Vitek, *Int. Mater. Rev.* **34**, 213 (1989)
38. V. Valvoda, M. Järvinen, *Powder Diffr.* **5**, 200 (1990)
39. G.X. Harris, *Lond. Edinb. Dublin Philos. Mag. J. Sci.* **43**, 113 (1952)
40. A.Z. Macknojia, J.V. Tran, M.P. McKinstry, J. Galindo, Y. Jin, S. Dowden, S.M. Patil, M.V. Pantawane, K.V. Mani Krishna, R. Banerjee, S.S. Joshi, N.B. Dahotre, *Mater. Des.* **241**(6), 112883 (2024)
41. S.M. Varahabhatla, M.S.K.K.Y. Nartu, S.A. Mantri, V. Chaudhary, K.M. Krishna, S.S. Joshi, R.V. Ramanujan, N.B. Dahotre, R. Banerjee, *Materialia* **30**, 101854 (2023)
42. G. Herzer, *IEEE Trans. Magn.* **25**, 3327 (2002)
43. B. Haghighat, M. Mokhles, M. Roldo, S. Birosca, *Prog. Addit. Manuf.* **10**, 11371 (2025)
44. H. Tiismus, A. Kallaste, A. Belahcen, M. Tarraste, T. Vaimann, A. Rassõlkin, B. Asad, P.S. Ghahfarokhi, *Energies* **14**, 1241 (2021)
45. N.J. Petch, *J Iron Steel Inst.* **174**, 25 (1953)
46. E. Hall, *Proc. Phys. Soc. B* **64**, 747 (1951)
47. N. Hansen, *Scr. Mater.* **51**, 801 (2004)
48. E. Hall, *Nature* **173**, 948 (1954)
49. A. Karolik, A. Luhvich, *J. Phys. Condens. Matter* **6**, 873 (1994)
50. E. Van der Voort, P. Guyot, *Phys. Status Solidi (B)* **47**, 465 (1971)
51. I. Bakonyi, *Eur. Phys. J. Plus* **136**, 410 (2021) □

Publisher's Note
Springer Nature remains neutral with regard to jurisdictional claims in published maps and institutional affiliations.